

27 dimensional nonlinear finite-element models. This research represents also a first step toward the development of a
28 rapid post-earthquake assessment approach for bridges with pile group foundations.

29 **Keywords:** pile group foundation; bridge scour; soil-pile interaction; seismic damage; post-earthquake residual
30 strength; ductility capacity; pushdown test.

31 **Introduction**

32 Reinforced concrete (RC) pile group foundations are extensively utilized in bridge engineering as they exhibit high
33 resistance to gravity loads and are easy to build. In a pile group foundation, all pile heads are connected together by
34 a cap. Many current specifications stipulate that pile group foundations should be designed to behave elastically under
35 design-level earthquakes based on the capacity design philosophy (Mander et al. 1998). However, pile damage is still
36 unavoidable when the pile-bridge system is subjected to unexpectedly large earthquakes (Kawashima et al. 2009; Wei
37 et al. 2008). In addition, scour is a main hazard for cross-river bridges (Wardhana and Hadipriono 2003). Due to the
38 riverbed scour (i.e., water-induced erosion), soil around the pile groups is eroded, resulting in the exposure of the pile
39 shafts near the cap (Shang et al. 2018; Wang et al. 2019c). The exposure of pile shafts reduce the lateral and vertical
40 load capacity of a pile group. In addition, the earthquake-induced damage tends to be transferred from column to piles
41 as the pile-supported bridges are subject to scour (Wang et al. 2015, 2019d, 2014). Therefore, the scoured pile groups
42 are generally subjected to a higher risk of earthquake-induced damage in earthquake-prone regions than their
43 counterparts without scour, particularly for older pile-supported bridges built prior to the implementation of the
44 capacity design approach. Pile damage could result in a permanent displacement of the pile group and the
45 superstructure, and reduce the vertical load-carrying capacity of the foundations (Bhattacharya et al. 2008; Lin and
46 Liao 1999; Wang et al. 2019b). Presently, experience-based post-earthquake inspections and engineering judgement
47 represent the main tools to estimate the remaining traffic capacity of a damaged bridge (O'Connor and Alampalli
48 2010). However, the unobservable pile damage located below the soil surface makes it difficult and time-consuming
49 to decide whether to reopen these damaged bridges for emergency traffic after an earthquake. Hence, it is essential to
50 quantitatively investigate post-earthquake load-carrying capacity of pile foundations under different damage levels
51 and understand their potential seismic failure mechanisms.

52 This study employs the quasi-static test method to investigate experimentally the behavior of damaged scoured

53 pile groups. This experimental method has been used extensively to investigate the ductile behavior and the load-
54 carrying capacity of structural specimens due to its simplicity and cost effectiveness (Wang et al. 2019a). This testing
55 technique was used to investigate the ductility capacity of single piles (Banerjee et al. 1987; Park and Falconer 1983),
56 and extended pile shafts (Chai and Hutchinson 2002). Lemnitzer et al. (2010) and Rollins et al. (2003, 2006) carried
57 out a series of quasi-static tests on pile groups, which were mainly focused on assessing the pile group effect. More
58 recently, Wang et al. (2016) and Liu et al. (2020) experimentally investigated the seismic failure mechanism of 2×2
59 and 2×3 pile group foundations considering the impact of pile shaft exposure. However, their test specimens consisted
60 of piles with a square section, whereas circular piles are more common in real-world applications. Research on the
61 post-earthquake load-carrying capacity of structural components has been relatively limited. Tasai (2000) investigated
62 the residual axial capacity of RC columns during shear degradation. Elwood and Moehle (2005) developed an axial
63 capacity model for shear-damaged columns. Terzic and Stojadinovic (2015a, 2015b; 2010) experimentally
64 investigated the post-earthquake residual load-carrying capacity of bridge columns under different ductility demand
65 conditions using a test technique named as “push-under”. They reported an approximate 20% reduction in vertical
66 load-carrying capacity of columns after undergoing a maximum displacement ductility demand of 4.5 and being
67 brought back to a zero residual displacement. However, since the damaged column specimens were re-centered before
68 performing the push-under test, the impact of permanent displacement on the residual load-carrying capacity of the
69 columns was not taken into account in their experiments. To the best of the authors’ knowledge, the residual load-
70 carrying capacity of pile group foundations under different lateral damage levels (corresponding to different
71 permanent deformations) has not been yet fully investigated in the literature, albeit it represents an indispensable
72 information to properly model a pile-supported bridge system after it is affected by a major earthquake.

73 This study aims to experimentally investigate the residual vertical load-carrying capacity of scoured RC pile
74 group foundations subjected to different damage levels. To this end, three 2×3 pile group foundation specimens (i.e.,
75 six circular piles connected by a cap) were constructed and tested in the indoor structural laboratory at Tongji
76 University, Shanghai, China. Each specimen was laterally loaded along its strong axis by imposing a series of cyclic
77 displacements until a predetermined damage state (or ductility level) was reached. A pushdown test was then
78 performed on these damaged specimens exhibiting a permanent lateral displacement. The seismic failure mechanism

79 and the ductility capacity of these pile group specimens were obtained. Finally, a quantitative evaluation for the post-
80 earthquake load-carrying capacity of pile groups under different ductility demand conditions was performed.

81 **Novelty and Relevance**

82 This study represents the first experimental investigation of the post-earthquake vertical load-carrying capacity of
83 scoured RC pile group foundations using quasi-static tests. The experimental data presented in this paper are
84 extremely valuable for modeling calibration and validation for future numerical investigations of soil-pile interaction
85 and post-earthquake load-carrying capacity evaluation of pile group foundations. This research represents a key step
86 toward the development of a rapid post-earthquake assessment approach for bridges with pile group foundations.

87 **Quasi-static Test Setup**

88 *Specimen configurations and instrumentations*

89 A 2×3 pile group was designed based on the capacity of lateral and vertical actuators, as well as on the indoor
90 laboratory space capabilities at Tongji University. Three identical specimens were built for the planned test. Figure 1
91 illustrates an overview of the pile group specimens, whereas Figure 2 presents some photographs of the test layout
92 for one of the physical specimens. Each specimen consisted of six circular piles with a length $H = 4.3$ m and a diameter
93 $D = 0.12$ m. These piles were placed in three rows along the lateral loading direction (i.e., east-west direction), and
94 their pile heads were connected together by a cap with dimensions of $1.5 \times 1.0 \times 0.6$ m, where 1.5 m is the length in
95 the loading direction, 1.0 m is the width perpendicular to the loading direction, and 0.6 is the thickness in the vertical
96 direction. The center-to-center pile spacing both in parallel and perpendicular to the loading direction was $3D$. In
97 order to model the scour effect, a portion of length 3.7 m ($30.83D$) out of the total length of each pile was embedded
98 in homogeneous sand with a relative density $D_r = 51\% \sim 58\%$, which represented a 0.6 m ($5D$) overall scour depth.
99 To minimize soil container boundary effects, the specimen was positioned in the central area of the container with an
100 inside dimension of 3.1 (length) × 1.5 (width) × 4.2 m (height). The distances between the outer piles and the soil
101 container walls in east-west and north-south directions were $9.42D$ and $4.25D$, respectively (see Figure 1b). As shown
102 in Figures 1a and 2b, the lateral load was provided by a servo-controlled hydraulic actuator (referred to as actuator
103 #1) with a 50-cm-stroke and 500-kN-capacity. One end of this actuator was mounted on the reaction wall and the
104 opposite end was connected to the center of the vertical surface of the pile group cap through bolts. To minimize the

105 influence of the self-weight of actuator #1 on the cap rotations, the front end of actuator #1 was hung from a cantilever
106 (mounted on the reaction wall) through two springs. Vertical loads were provided by a 200-cm-stroke/1600-kN-
107 capacity servo-controlled hydraulic actuator (referred to as actuator #2), whose upper end was suspended from a
108 bidirectional sliding rail that was installed on a 3000-kN-capacity counterforce frame, as shown in Figure 2a.
109 Therefore, actuator #2 remained vertical during all loading phases since its upper end synchronously moved with the
110 specimen in the horizontal direction.

111 Figures 1 and 2 also display the instrumentations used in the test. Three 1000-mm-length linear variable
112 displacement transducers (LVDT) were installed on the cap to trace its lateral displacements along the loading
113 direction. Among the three LVDTs, the middle one was used to control the lateral displacement loading, whereas the
114 other two were used to indirectly trace the cap rotations through geometric transformation of the data measured by
115 them. The cap rotation was also directly measured by one inclinometer attached on the top of the cap, as shown in
116 Figure 1b and Figure 2e. The strain of longitudinal rebars at the eastern and western edges of the pile sections were
117 monitored by 16 pairs of strain gauges, and their distribution along the pile shaft are shown in Figure 1c. These strain
118 gauges were also used to calculate the cross-section curvature during the tests. Since strain gauges were expected to
119 malfunction for highly nonlinear behavior of the rebars they were attached to, linear potentiometers were also pairwise
120 placed along the aboveground piles in the regions of length $3D$ below the pile heads to trace the average section
121 curvatures. Detailed transformation procedures to calculate the section curvature from the displacement measured by
122 linear potentiometers can be found in the literature (Zhou et al. 2019). Due to the limited number of data acquisition
123 channels and sensors, both strain gauges and linear potentiometers were placed only on three of the six piles, which
124 are highlighted in gray color in Figure 1b. In addition, four laser sensors (identified by red stars in Figure 1b) were
125 fixed on an external steel pipe frame (Figures 2a and 2d) and placed over the cap top to measure its vertical
126 displacement. The mean values of the cap displacements in the vertical direction measured by the four laser sensors
127 in pushdown phase are considered representative of the vertical displacement of the specimen, thus eliminating the
128 influence of the cap rotations.

129 ***Pile reinforcements and section moment-curvature analysis***

130 As shown in Figures 1c and 1d, six 6-mm-diameter longitudinal rebars were annularly assembled in the pile

131 sections and provided a longitudinal steel reinforcement ratio of 1.5%. All longitudinal steel reinforcement bars in
132 each pile were extended 58 cm into the cap to ensure a reliable pile-cap connection. The core concrete of the piles
133 were spirally confined by 3.5-mm-diameter galvanized-iron-wires (GIWs) spaced at 35 mm, leading to a transverse
134 steel reinforcement ratio of 1.215%. The thickness of the concrete cover was 13 mm, which was measured from the
135 outside face of the GIWs to the pile surface. Six plain concrete cylinders with a height of 300 mm and a diameter of
136 150 mm, cast on the same day when the pile group specimens were fabricated, were tested to determine the elastic
137 modulus and peak strength of the concrete by compression tests (i.e., three specimens for the former and other three
138 specimens for the latter). Three rebars and three GIW specimens were also tested to determine their mechanical
139 parameters via tensile tests. These tests were performed on the sixth day before the commencement of the quasi-static
140 test. Table 1 lists the average values and the coefficients of variation (provided as percentage in parentheses) of the
141 measured mechanical parameters for the concrete and steel reinforcements employed in the specimen fabrication.

142 A moment-curvature analysis for the pile section was performed by using the OpenSees software framework
143 (McKenna 2011). The pile section was modeled by using a zero-length element with fiber discretization of the cross-
144 section. Different constitutive models were assigned to fibers corresponding to concrete cover (unconfined concrete),
145 concrete core (GIW-confined concrete), and longitudinal steel rebars. In particular, the concrete fibers were modeled
146 by using the uniaxial constitutive model denoted in OpenSees as *Concrete01*, which corresponds to the Kent-Scott-
147 Park model with zero strength in tension (Scott et al. 1982). This model can better represent the post-peak degrading
148 slope and stress-strain behavior of GIW-confined concrete (Terzic and Stojadinovic 2015a). The strains corresponding
149 to peak compressive strength and crushing strength of the unconfined concrete were taken as 0.002 and 0.006,
150 respectively (Barbato et al. 2010), as they were not measured in the testing of the concrete cylindrical specimens. The
151 peak strength of the confined concrete was taken as 29.05 MPa, which was calculated by using the formula
152 recommended by Scott et al. (1982). The strain at peak strength and the ultimate strain of the confined concrete were
153 taken equal to 0.0037 and 0.021, respectively, based on the experimental data of short columns presented in last
154 section. The residual strengths of both confined and unconfined concrete were taken as 20% of their corresponding
155 peak strengths. The longitudinal rebars were modeled by using the uniaxial constitutive model denoted in OpenSees
156 as *Steel02*, which corresponds to the Menegotto-Pinto model with isotropic strain hardening (Filippou et al. 1983). A

157 quasi-static analysis was performed by using a displacement-controlled pattern, with a rotation increment equal to
158 5.0×10^{-3} rad. The NewtonLineSearch algorithm with a tolerance of 0.8 in OpenSees was used to solve the resulting
159 non-linear equations (Mazzoni et al. 2006).

160 Figure 3 presents the moment-curvature results for the pile section subject to an axial load ratio of 5%, which
161 corresponds to the axial load ratio of the test piles under dead loads only. The axial load ratio is defined here as the
162 ratio between the applied axial load and axial strength of the pile obtained as the product of the unconfined concrete
163 peak strength and the pile cross-section gross, consistently with the definition used in the literature (Lam et al. 2003).
164 Wang et al. (2016) and Liu et al. (2020) reported that the yielding curvature of a pile section is not sensitive to axial
165 load variations. By contrast, they found that the ultimate curvature is highly dependent on axial load variations. This
166 study employs the yielding curvature of a pile section to identify the yielding sequence of piles. Therefore, although
167 the axial loads applied on piles generally vary when a pile group is subjected to lateral loads, the axial force variation
168 was not taken into account in the moment-curvature analysis of the pile section, because its effect on the pile yielding
169 curvature is negligible. The analysis results indicate that the ultimate curvature of the pile section is 0.838 rad/m and
170 corresponds to crushing of the core concrete, which occurs before the rupture of the longitudinal steel rebar. Based
171 on the computed moment-curvature curve, the equivalent yielding curvature of the pile cross-section was estimated
172 as 0.045rad/m. This curvature was obtained from the idealized bilinear moment-curvature curve (identified by dashed
173 lines in Figure 3), and corresponded to the curvature of the intersection between the elastic line (with slope equal to
174 the secant stiffness between the origin and the point of first yielding on the numerical moment-curvature curve) and
175 the horizontal line corresponding to fully-plasticized cross-section. Hereinafter, the equivalent yielding curvature is
176 used to determine if a cross-section has reached plasticization.

177 ***Soil properties and placement***

178 Dry yellow silicon sand from Shanghai, China, was used as the surrounding soil for the test piles. The particle
179 size distribution for this sand is shown in Figure 4. The average grain size of the sand, D_{50} , was 0.293 mm, and the
180 uniformity coefficient C_u (which is defined as the ratio of the grain size corresponding to 60% and 10% passing
181 materials, D_{60}/D_{10}) is 2.5. The measured maximum and minimum dry bulk densities were 17.23 kN/m³ and 14.01
182 kN/m³, respectively. The moisture content of the test sand was 0.16%.

183 Before the placement of the sand, the precast pile group specimen was placed first in the soil container and
184 supported vertically on one 4-cm-thickness square steel plate mounted at the bottom of the container. It is pointed out
185 that this configuration of the experiment was representative of a pile group with end bearing on rock/stiff substrata.
186 To ensure a uniform compaction of the soil, the 3.7-m-depth sand was placed sequentially in thirteen layers (i.e., the
187 first twelve layers with an approximately same thickness of 30 cm and the last layer with a thickness of 10 cm). Each
188 sand layer was artificially compacted using wooden hammers. Note that slight differences between the actual and
189 target compaction thickness for each soil layer were inevitable. This thickness variability resulted in a slight variation
190 of the relative density of sand, which was contained between 51% and 58%.

191 *Test procedure*

192 Figure 5 presents the test loading protocol. A three-phase test loading protocol, inspired by the test loading
193 procedure used in Terzic and Stojadinovic (2015a), was adopted to investigate the residual load-carrying capacity of
194 the three pile group specimens at different damage states, as well as to identify their failure mechanism. The protocol
195 used in this study included lateral loading (first and second phases of the test) followed by the pushdown test (third
196 and last phase of the test). In the first phase, lateral cyclic displacements following the predesigned loading protocol
197 at a constant rate of 0.5 mm/s were imposed on the pile cap to produce the target damage levels, as listed in Table 2
198 for the three specimens. In particular, the lateral loading protocols for specimens #1, #2, and #3 were selected so to
199 reach the first-yielding of the belowground pile shafts, the onset of the lateral strength degradation (i.e., by loading
200 the specimen up to its peak lateral strength), and a 15% degradation of the lateral strength, respectively. The maximum
201 lateral displacement levels applied to specimens #1, #2, and #3 were 35 mm, 70 mm, and 100 mm, respectively. The
202 values of the lateral displacement levels corresponding to the selected damage states of interest were based on the
203 data obtained from testing specimen #3 before the other two specimens, i.e., by measuring the displacements at which
204 first-yielding of the belowground pile shaft and onset of lateral strength degradation took place, and by interrupting
205 the test as soon as a 15% degradation of the lateral strength was observed. All specimens were returned to a zero-
206 displacement state of their cap at the end of the first loading phase. The second loading phase was used to simulate
207 the residual deformation state of pile group foundations after an earthquake. Each specimen was loaded again to the
208 maximum displacement level reached in the first loading phase, and then unloaded to a zero-lateral force state (i.e.,

209 the so-called residual displacement state). After that, the horizontal actuator (actuator #1) was carefully separated
210 from the specimen after unscrewing the nuts from the cap-actuator connections. In the first and second lateral loading
211 phases, the initial axial force on the piles was set equal to an axial load ratio of 5% and was provided by the
212 combination of the load applied by actuator #2 (i.e., 62.0 kN) and the cap weight (i.e., 23.4 kN). In the third and last
213 loading phase, a pushdown test on the damaged specimens at their residual deformation state was performed through
214 actuator #2 using a displacement-controlled monotonic loading with a constant rate of 1.0 mm/min.

215 *Verification of soil container boundary conditions*

216 In order to ensure the validity of the experimental results, the boundary conditions provided by the soil container
217 need to correspond to a negligible lateral soil pressure. Two soil pressure sensors were attached on the west side (i.e.,
218 along the loading direction) and the south side (i.e., perpendicularly to the loading direction) of the soil container
219 walls at the depth of 4D and 2D, respectively. An additional soil pressure sensor was installed on the leading pile
220 along the loading direction at the depth of 4D. Figure 6 compares the peak soil pressure measured on the leading pile
221 and the container walls at different displacement levels. It is observed that the boundary effects in this test can be
222 neglected, as the peak lateral soil pressure measured on the west side and the south side of the container wall were
223 equal to 0.017 MPa and 0.003 MPa, respectively, which were negligible when compared to the peak soil pressure
224 measured on the leading pile (i.e., 0.288 MPa). These results also indicate that the soil domain dimensions of 9.42 D
225 and 4.25 D along and perpendicular to the loading direction, respectively, were sufficient to minimize the boundary
226 effects in the soil-pile interaction tests performed for the present study.

227 **Seismic Failure Mechanism and Ductility Capacity**

228 *Pile group hysteretic behavior*

229 The hysteretic lateral force versus displacement responses for the three specimens are shown in Figure 7a, and the
230 response envelope profiles of each specimen are plotted in Figure 7b. Because displacement-force responses for each
231 specimen under three cyclic loadings with the same displacement amplitude were almost identical, only the responses
232 corresponding to the second cycle of each displacement amplitude are presented herein for the sake of clarity. It is
233 observed that the responses of the three specimens almost coincide for the same displacement levels, and that the
234 lateral forces at maximum displacement of each specimen in both push and pull directions are very close (i.e., +28.3

235 kN and -31.3 kN for specimen #1, +28.3 kN and -31.5 kN for specimen #2, and +27.5 kN and -27.4 kN for specimen
236 #3). The small variability of these results shows that the mechanical properties and the sand condition are fairly
237 consistent among all specimens. In addition, the wide hysteretic loops observed in these tests indicate a high ductility
238 and a stable response for the pile group.

239 *Pile curvature distribution and plastic hinge developments*

240 Figure 8 presents the section curvature distributions along the pile shafts at the peak displacements for different
241 loading cycles (i.e., 10, 20, 30, 40, and 50 mm) in the push and pull directions, respectively. Note that a few strain
242 gauges in the potential plastic hinge region of the piles malfunctioned after yielding of the longitudinal reinforcement,
243 causing the loss of information on the corresponding pile section curvatures. In particular, the loss of belowground
244 strain gauges started between displacement levels of 40 and 50 mm in a few locations (characterized by large
245 curvatures) on the leading and trailing piles below soil surface, and then expanded rapidly to other locations for larger
246 displacement levels. Therefore, Figure 8 presents the curvature distributions along the pile shafts only up to a
247 displacement level of 50 mm. For the 50 mm displacement level, the locations where the strain gauges malfunctioned
248 are marked by the symbol “×”, and report the last curvature value recorded before the loss of the corresponding strain
249 gauge. As soon as the strain gauges at pile heads were disabled, the pile head curvature was calculated from the data
250 measured by linear potentiometers. These values are identified by circles in Figure 8. It is pointed out that the outer
251 piles in the pile group alternately played the role of leading and trailing piles under cyclic loads, i.e., piles 1 and 3 in
252 each specimen acted as the leading and trailing piles in the push direction, respectively; whereas they correspondingly
253 converted to trailing pile and leading pile in pull direction. As shown in Figure 8, a similar curvature distribution of
254 the pile shaft was recorded in correspondence of the same lateral displacement level when pile 1 and pile 3 acted as
255 the leading (or trailing) piles, respectively.

256 The equivalent yielding curvature of the pile section, which was found to be equal to 0.045 rad/m from the
257 moment-curvature analysis, is also represented in Figure 8 as vertical dashed lines. This quantity is used as the basis
258 to identify whether the pile section yields at a given displacement level. It is observed that the lateral loading phase
259 of the test produced two plastic hinges on each pile in the scoured pile group: the first hinge was located at the pile
260 head, whereas the second hinge occurred on the pile shaft below the ground surface, and the contraflexure point

261 (indicated by filled markers) was located near the ground surface, as shown in Figure 8. This phenomenon also implies
262 that the three piles standing in a line along the lateral loading direction formed a frame-like structure. By comparing
263 the curvature envelopes of different piles at the same displacement level, it is observed that the curvature of each pile
264 section at the same elevation decreased from the leading to the middle pile and from the middle to the trailing pile.
265 This result implies that the leading pile carried a larger proportion of the lateral loads on the pile group foundations
266 than the middle and trailing piles, due to the pile group effect. This phenomenon was also reported by Rollins et al.
267 (2005). In addition, the embedded depth of the maximum curvature for a belowground pile section gradually increased
268 when going from the leading (i.e., between -5D and -6D), to the middle (i.e., between -7D and -8D), to the trailing
269 (i.e., between -9D and -10D) piles. Within the same pile, the embedded depth of the belowground section with
270 maximum curvature tended to decrease with the increase of the displacement levels. It is also observed that the section
271 curvature at the pile head was larger than that of all other sections along the pile shaft under any displacement level.
272 These findings indicate that the leading pile, and especially its pile head, was more prone to seismic damage than the
273 other piles, as both the first aboveground and first belowground plastic hinges originally occurred on it. This
274 conclusion is also consistent with the experimental results reported by Liu et al. (2020).

275 In the test performed for this study, the pile heads of the leading piles (i.e., piles 1 and 3) were the first locations
276 to reach yielding at a displacement level of approximately 20 mm. The first belowground plastic hinges also occurred
277 on the leading piles, as the lateral displacement increased to 35 mm. After that, the second belowground plastic hinge
278 was formed on the middle pile at a displacement level of approximately 50 mm. Table 3 lists the measured pile head
279 curvatures at displacement levels of 35 mm, 70 mm, and 100 mm. Also for these results, in general, it is observed
280 that the curvature of the pile head gradually decreased from leading, to middle, to trailing piles for a given
281 displacement level. At the displacement of 100 mm, the pile head of the leading pile reached its ultimate curvature,
282 which corresponds to the condition of core concrete crushing.

283 ***Displacement ductility of pile group specimens***

284 The local section curvature ductility cannot fully describe the global damage state of a pile group foundation
285 because multiple plastic hinges can occur on the different piles, as also shown in the present study. Therefore, Blanco
286 et al (2019) proposed the displacement ductility (μ_D) as a global damage index for a pile group, which is defined as:

$$\mu_D = \frac{\Delta}{\Delta_y} \quad (1)$$

287 where Δ_y is the horizontal displacement of the cap center corresponding to the first section yielding of any pile in
 288 the pile group, and Δ represents the cap horizontal displacement corresponding to a specific damage state. In this
 289 study, a section yielding is identified when the curvature of a section reaches the equivalent yielding curvature as
 290 determined by the cross-sectional moment-curvature analysis reported in Figure 3. In this test, the yield displacements
 291 were measured for the three specimens as 20.0 mm, 19.8 mm, and 20.1 mm, respectively. Given the small variations
 292 among the two specimens (i.e., with differences smaller than 1 mm), the average value $\Delta_y = 20$ mm was used to
 293 calculate the experimental displacement ductility of the three specimens. Table 4 lists the measured displacement
 294 ductility of the specimens at different damage states, as well as the maximum curvature ductility of the first
 295 aboveground plastic hinge in the leading pile. It is observed that the pile group specimens exhibited a considerable
 296 displacement and curvature ductility capacity.

297 *Pile-cap rotations and pile head crack developments*

298 Figure 9 presents the measured peak and residual cap rotation angles of specimen #3 at different lateral
 299 displacement levels. The residual cap rotation is defined here as the tilt angle of the pile group at the zero-lateral force
 300 state. To check the measurement accuracy of the cap rotation, the cap rotations measured by using the inclinometer
 301 were compared with the results calculated from the LVDT data via geometric transformation. In general, very similar
 302 cap rotation values were obtained by these two measurement methods. The recorded data indicate an approximately
 303 symmetrical cap rotation-peak displacement relation in the push and pull directions.

304 Two fitting formulas for the peak and residual cap rotations with respect to the displacement ductility are
 305 proposed as follows:

$$\theta_p = \frac{7}{5000} \mu_D \quad 0 \leq \mu_D \leq 5 \quad (2)$$

$$\theta_r = \begin{cases} 0 & 0 \leq \mu_D < 2 \\ \frac{1}{5000} (\mu_D^2 - 2\mu_D) & 2 \leq \mu_D \leq 5 \end{cases} \quad (3)$$

306 where θ_p and θ_r denote the peak and residual cap rotations, respectively. These equations could be used to predict
 307 the cap peak and residual rotation for pile groups exhibiting a specified ductility. However, these equations should

308 also be validated with additional experimental data, including at a minimum different configurations for the pile
309 groups, different levels of scour, and different soil types and relative densities.

310 The progression of cracking in the aboveground portion of the pile shafts was also investigated through direct
311 observation and measurements. Overall, the cracks progressed in a similar fashion in the three specimens. Initially,
312 three horizontal hairline cracks with an average spacing of 6 cm (0.5D) occurred in the regions of length 2D below
313 the pile head of the leading piles at the displacement level of 10 mm ($\mu_D = 0.5$). At this displacement level, two
314 similar cracks occurred also on the middle pile heads. Subsequent loadings produced additional cracks on piles, which
315 were horizontally distributed in the regions of length 3D below the pile heads with a spacing of 3-6 cm. After the
316 lateral displacement exceeded 40 mm ($\mu_D = 2.0$), almost no new horizontal cracks occurred in the aboveground
317 portion of the piles. In addition, no diagonal cracks were observed during the lateral loading phase.

318 A clip gauge was employed to record the variation of the main crack of a leading pile within the displacement
319 ductility range between 0.75 and 1.75. The feasibility of using clip gauges to record the crack progression was
320 confirmed by Guan et al. (2017). The clip gauge was located at approximately 8 cm below the pile head on the leading
321 pile. Due to an insufficient installation space for the clip gauge, it was not possible to measure the progression of
322 another crack observed near the pile head, even though this crack seemed wider than the measured one under visual
323 inspection. Figure 10a shows the variation of the crack width with respect to the applied lateral force for different
324 lateral displacement levels. Since the lateral force-crack width curves for 15 mm and 20 mm of lateral displacement
325 are very similar, the former is not shown for the sake of clarity. It is observed that, after opening during the loading
326 phases, the crack gradually reclosed during the unloading phases. Figure 10b compares the measured crack widths at
327 the maximum loading value, at the residual displacement state (i.e., zero-lateral load condition), and at the zero-cap
328 displacement state. For clarity, the crack widths at these different states are marked on the curve corresponding to 35
329 mm of lateral displacement in Figure 10(a). It is observed that the zero-lateral force crack width was always larger
330 than the corresponding zero-cap displacement crack width at the same displacement level. This result was expected
331 because the zero-lateral force conditions correspond to residual deformations, which are removed when considering
332 the zero-cap displacement conditions. This finding suggests that using the crack width corresponding to zero-cap
333 displacement state can significantly underestimate the residual-crack damage, which is consistent with the findings

334 reported by Guan et al. (2017).

335 Moreover, the residual cracks started forming as soon as the pile group reached yielding (i.e., for displacement
336 ductility approximately equal to 1), as shown in Figure 10b. Similar observations were also made by Yeh et al. (2002).
337 In the present test, the measured crack widths before the cross-section yielding of the belowground pile shaft were
338 0.61 mm at the maximum value, and 0.28 mm at the zero-lateral force state (i.e., the residual crack width was equal
339 to 0.28 mm). Therefore, only hairline residual cracks (i.e., barely visible to the naked eye) occurred on the piles before
340 the formation of any belowground plastic hinge. Under these conditions, retrofitting of the piles would not be required.
341 In fact, according to Hose and Seible (1999) and Guan et al. (2017), residual cracks with a width smaller than 0.3 mm
342 are barely visible, correspond to a fully operational condition for a RC structure, and do not require any repair.

343 *Summary of observed damage and residual displacements of specimens*

344 Table 5 summarizes the global performance and local damage descriptions for the three pile group specimens at
345 different damage states. Figure 11 shows some pictures of the aboveground portions of the pile group at the zero-
346 lateral force state (or residual displacement state) corresponding to each damage state. In this study, only hairline
347 residual cracks were detected in the pile head regions when specimen #1 reached the belowground cross-section
348 yielding for the pile shafts (corresponding to $\mu_D = 1.75$). Limited cover concrete spalling was observed on the pile
349 heads of the leading and middle piles when specimen #2 underwent the onset of lateral strength degradation
350 (corresponding to $\mu_D = 3.5$). Finally, extensive cover concrete spalling was observed on the pile heads of the
351 leading and middle piles when specimen #3 experienced a 15% degradation of the lateral strength (corresponding to
352 $\mu_D = 5.0$). In correspondence to this damage state, some local core concrete crushing was also observed on the
353 leading piles. In addition, the pile damage caused a permanent lateral displacement on the pile cap, which was equal
354 to 14 mm, 40 mm, and 68 mm for specimens #1, #2, and #3, respectively, corresponding to residual drift ratios of
355 1.16%, 3.33%, 5.66%, respectively. The residual drift ratio herein is defined as the ratio between the permanent cap
356 displacement in the horizontal direction and the distance between the cap top surface and the soil surface (i.e., 1.2 m
357 or 10D). It is observed that the residual cap rotations were always very small, with a maximum value of 3.9×10^{-3}
358 rad for specimen #3. Since the pushdown test needed to be performed on these laterally-damaged pile groups, the
359 belowground pile conditions were not inspected at the end of the lateral loading phases and no direct observation of

360 the belowground damage states is available.

361 An increasing gap between the leading pile and its surrounding soil was observed for increasing displacement
362 levels. This phenomenon was caused by the lateral compaction of the sand in front of the leading piles. As shown in
363 Figure 11, this compaction resulted in a clearly visible localized hole near and in front of the leading piles, while a
364 slight global sand settlement was also observed in the test around the middle piles. For example, for the specimen #3,
365 the sand hole at east side had a depth of approximately 18 cm and a width of approximately 80 cm, and the global
366 sand settlement around the middle piles was approximately 7.2 cm (i.e., 0.6D). A similar phenomenon was also
367 reported by Wang et al. (2016). Note that since the residual deformation of the pile group at each damage state was
368 towards the push direction (or west side), the final local hole at the east side was wider and deeper than that at the
369 west side. By contrast, the width of the residual cracks on the aboveground portion of the pile shafts at the east side
370 was smaller than that at the west side. As shown in Figure 11, the sand hole at the east side gradually became wider
371 and deeper for the three damage states.

372 **Post-earthquake Load-carrying Capacity of Pile Group at Different Damage States**

373 *Vertical load-carrying capacity estimation for the undamaged pile group specimen*

374 The vertical load-carrying capacity of the undamaged pile group specimens (referred to as initial vertical load-
375 carrying capacity hereinafter) was estimated in order to provide a basis for comparison of the test results on the
376 damaged pile group specimens. This estimate was performed indirectly because of the limited capacity of actuator #2
377 (i.e., 1600 kN), which was deemed insufficient to reach the expected peak vertical load-carrying capacity of the $2 \times$
378 3 pile group considered in this study. In particular, the initial vertical load-carrying capacity of the pile group specimen
379 was estimated as six times the strength of a single pile. Due to the constraints imposed by the surrounding soil and
380 the cap, the piles in the studied pile group specimen formed a frame-like structure, and the boundary condition of the
381 pile at the soil surface is closer to a hinged end, as indicated by the position of the contraflexure point reported in the
382 figure 8. When the undamaged pile group is subject to vertical load only, the horizontal displacement of each pile
383 could be restrained by whole pile group. Therefore, each pile under axial loads could be analyzed as an equivalent
384 column with an approximately fixed end at the cap bottom and hinged end at the soil surface. Due to the loading
385 condition corresponding to vertical load only for the undamaged pile group, each pile in the pile group specimen was

386 equivalent to an axially loaded column with a length equal to 60 cm (i.e., 5D) and an effective length coefficient
387 smaller than or equal to 1. Because of the small length-to-diameter ratio (corresponding to a slenderness smaller than
388 or equal to 20), each pile was considered as a short column. Thus, the strength of the individual pile was estimated
389 both experimentally through axial compression tests on three short columns, and numerically through a finite-element
390 sectional analysis. The length of the short column's physical specimens was selected equal to 3D based on the
391 capabilities of the available experimental testing equipment.

392 The three short columns had a length equal to 36 cm, and a diameter equal to 12 cm. These columns had the
393 same transversal and longitudinal steel reinforcements used for the piles in the pile group specimens, and were
394 fabricated on the same day of and with the same materials used for the pile group specimens. The short columns were
395 subjected to a displacement-controlled axial loading with a displacement of 0.216 mm/minute (corresponding to a
396 strain rate of $1 \times 10^{-5} \text{ s}^{-1}$). The experimental axial force-axial strain response of the three columns is shown in Figure
397 12. The peak strengths of the three columns were 265 kN, 291 kN, and 283 kN, respectively, corresponding to an
398 average peak strength is 280 kN. A numerical analysis of the axial behavior of the same pile section was also
399 performed in OpenSees. The modeling details, analysis type, and material parameters used to describe the confined
400 and unconfined concrete and longitudinal steel rebars were identical to those used in the moment-curvature analysis
401 of the pile section. To account for accidental eccentricity, an eccentricity-to-diameter ratio of 0.05 (corresponding to
402 an axial load eccentricity equal to 6.0 mm) was assumed in the axial section analysis for the pile section, based on
403 the recommendation of ACI 318 for columns with spirals (ACI 2014). The numerical axial force-axial strain response
404 for the pile section is also shown in Figure 12. The numerical analysis provided a peak strength for the section equal
405 to 286 kN, which is consistent with the experimental results obtained from the short columns. Based on these results,
406 the initial vertical load-carrying capacity of the 2×3 pile group specimen was assumed equal to 1680 kN, i.e., 6 times
407 the average peak strength obtained from the experimental results of the axial compression tests performed on the
408 short columns.

409 ***Post-earthquake vertical load-carrying capacity and failure mode***

410 The residual vertical load-carrying capacity of the laterally-damaged pile group specimens (i.e., with the
411 permanent lateral displacement induced by the cyclic loading phases) were evaluated via a pushdown test. Figure 13

412 plots the applied vertical load and the cap lateral displacement versus the vertical displacement increment for the
413 three pile group specimens. The initial vertical load of 62 kN corresponding to zero vertical displacement increment
414 represents the dead load applied to the pile group. Figure 14 shows some pictures of the physical specimens after
415 completion of the test and removal of the surrounding soil.

416 The residual vertical load-carrying capacity of specimen #1 was 1505 kN, which corresponded to 89.6% of the
417 initial vertical load-carrying capacity of the undamaged 2×3 pile group. It is observed that the lateral displacement of
418 the pile cap slightly decreased during the vertical loading phase until the peak vertical force was reached. After
419 reaching the peak resistance and maintaining it for approximately 1 mm of vertical displacement increment (Figure
420 13a), the vertical resistance of specimen #1 suddenly dropped. As shown in Figure 14(a)-1, the pile heads of the three
421 piles on the south side of the specimen failed in shear, whereas the three piles in the north side of the specimen
422 exhibited a flexural failure mode, which was induced by the cap tilt along the north-south direction.

423 The residual vertical load-carrying capacity of specimen #2 was 882 kN, which corresponded to 52.5% of the
424 initial vertical load-carrying capacity of the pile group. It is observed that the cap lateral displacement for this
425 specimen remained almost constant until the peak vertical resistance was reached at approximately 4.3 mm. After the
426 peak vertical strength was reached, the lateral displacement of the cap started increasing significantly until the
427 specimen suddenly failed in flexure (see Figure 14(b)-1), with the cap rotating vertically about the north-south axis
428 (Figure 14(b)-2) and twisting about the vertical axis (Figure 14(b)-3). The twisting of the cap is highlighted by the
429 non-parallel traces of the container wall and the cap edge, which are shown by dashed red lines in Figure 14(b)-3.

430 The residual vertical load-carrying capacity of specimen #3 was 440 kN, which corresponded to 26.2% of the
431 initial vertical load-carrying capacity of the pile group. Figure 14(c) shows some pictures of the post-test conditions
432 of the physical specimen. This specimen failed following a flexural failure mode with a pronounced rotation of the
433 cap in the north-south direction. As shown in Figure 13(b), the cap lateral displacement gradually increased from the
434 initial residual displacement for increasing vertical displacement.

435 As shown in Figure 14(c)-2, the confinement effect provided by the sand inhibited the spalling of cover concrete
436 in the plastic hinge regions of the belowground pile shafts, even after the pile shaft suffered severe flexural damage.
437 For specimens #2 and #3, the flexural deformation gradually decreased from the piles in the first row to those in the

438 third row with respect to the direction of the cap residual displacement. The embedded depth of the plastic hinge
 439 centers on the belowground pile shafts were approximately 4D, 5D, and 6D in sequence, which corresponded to
 440 shallower depths than those obtained from curvature measurements during the cyclic loading phases of the test and
 441 reported in Figure 8. This phenomenon was observed because specimens #2 and #3 experienced relatively large lateral
 442 displacements (i.e., more than 12 cm) induced by the vertical loads applied during the pushdown phase, and the
 443 embedded depth of the belowground plastic hinge in each pile tended to decrease for increasing lateral displacement
 444 levels. It is noteworthy that no cracks were observed on the piles at a depth higher than 14D from the soil surface.
 445 Finally, by using a plumb bob hung from the bottom of the cap (see Figures 14(a)-3 and 14(c)-3), it was observed that
 446 the belowground portions of the pile shafts remained almost vertical and undamaged in specimen #1, whereas they
 447 remained practically vertical and undamaged below the belowground plastic hinges in specimens #2 and #3. Therefore,
 448 it is concluded that the pile damage induced by lateral loads were mainly concentrated in the pile heads and in the
 449 upper portions embedded in the sand (i.e., between 3D and 10D below the soil surface) for the scoured pile groups.
 450 This pile damage led to a permanent displacement and tilt on the cap, and dominated the residual vertical load capacity
 451 and the vertical failure mode of the pile group foundations.

452 ***Vertical load-carrying capacity degradation***

453 The test results demonstrated that the pile damage after the cyclic loading phases affected significantly the
 454 residual vertical load-carrying capacity of the pile groups and their failure modes induced by vertical loads. Figure
 455 15 illustrates the experimentally-derived vertical load-carrying capacity degradation (expressed as vertical peak
 456 strength normalized by the estimated peak strength of the undamaged pile group) as a function of the peak
 457 displacement ductility of the pile groups. The data points obtained from the pushdown tests were fitted by using a
 458 piecewise linear function given by:

$$\frac{P_R}{P_0} = \begin{cases} 1 & 0 \leq \mu_D \leq 1 \\ 1.185 - 0.185\mu_D & 1 < \mu_D \leq 5 \end{cases} \quad (4)$$

459 where P_R and P_0 denote the residual and initial vertical load-carrying capacity of the pile group, respectively. This
 460 proposed equation is based on two assumptions: (1) no losses in the vertical load-carrying capacity of the pile groups
 461 are suffered if the displacement ductility is less than or equal to 1.0; and (2) the degradation of the vertical load-

462 carrying capacity is assumed linear in the range $1.0 \leq \mu_D \leq 5.0$. The high value of the coefficient of determination
463 $R^2 = 0.996$ suggests that the linear model proposed in this study is appropriate. It is noteworthy that Equation 4 is
464 valid only for the specific conditions representing the experimental tests reported in this paper. However, the proposed
465 vertical load-carrying capacity degradation curve could represent a starting point to develop more general curves to
466 predict the residual vertical load-carrying capacity of damaged scoured pile groups, e.g., for bridge rating and post-
467 earthquake rapid assessment applications. However, in order to develop such curves, additional experimental results
468 are needed considering, at a minimum: different pile configurations, sizes, and numbers; different material properties;
469 different scour depths; and different soil profiles and conditions.

470 **Conclusions**

471 This study investigated the seismic failure mechanism and post-earthquake vertical load-carrying capacity of scoured
472 pile group foundations. Three identical 2×3 pile group specimens were embedded in homogeneous sand, compacted
473 to a relative density $D_r = 51$ -58% with an overall scour depth of 5D, where D = 12 cm denotes the diameter of a single
474 pile. The soil container had dimensions of 310 cm and 150 cm in the directions parallel and perpendicular to the cyclic
475 loading direction. This configuration allowed a distance of all piles of at least 113 cm (9.42D) and 51 cm (4.25D)
476 from the soil container boundary in the directions parallel and perpendicular to the cyclic loading direction. It was
477 shown that these distances were sufficient to render almost negligible the boundary effects on the pile-soil interaction.
478 The three specimens were first subjected to a horizontal cyclic loading applied to pile cap to simulate the effects of
479 earthquake loads. The maximum intensity of the cyclic loading was selected to produce three different predetermined
480 damage states. The damaged pile group specimens (i.e., with a residual lateral displacement) were then subjected to
481 a pushdown test to evaluate their residual load-carrying capacity. This study produced the following main findings:

482 (1) For the considered scoured pile group, the piles aligned along the lateral load direction formed a frame-like
483 structure due to the constraints imposed by surrounding soil and the pile-cap connection. Each pile in the pile
484 group exhibited two potential plastic hinge locations: the first one was located at the pile head, and the second
485 one was located in the belowground portion of the pile shaft. Both the first aboveground and first belowground
486 plastic hinges occurred on the leading piles when the scoured pile groups were subjected to the cyclic loading
487 representing the earthquake loading effects. Thus, the test results presented in this study suggest that the leading

488 piles are more prone to seismic damage than internal piles in pile group foundations. In addition, the embedded
489 depth of the belowground plastic hinges gradually increased from leading, to middle, and to trailing piles. For a
490 given pile, the embedded depth of the belowground plastic hinge decreased for increasing lateral displacement
491 levels.

492 (2) The three pile group specimens experienced a degradation of their vertical load-carrying capacity of 10.4%,
493 47.5%, and 73.8%, corresponding to a peak displacement ductility of 1.75, 3.5 and 5.0, respectively. The failure
494 mode under vertical loading changed for different residual cap lateral displacements, with a shear failure for
495 specimen #1 (corresponding to a peak displacement ductility of 1.75), a mixed flexural-torsional failure for
496 specimen #2 (corresponding to a peak displacement ductility of 3.5), and a flexural failure for specimen #3
497 (corresponding to a peak displacement ductility of 5.0).

498 (3) The damage induced on the piles by the cyclic loading resulted in a linear degradation of the residual vertical
499 load-carrying capacity of the pile groups. In particular, the residual vertical load-carrying capacity of the pile
500 group specimens decreased linearly for increasing peak displacement ductility larger than 1.0. A piecewise linear
501 function was fitted to the experimental results.

502 It is noteworthy that this paper focuses mainly on the seismic failure mechanism and the residual vertical load-
503 carrying capacity of 2×3 scoured pile groups in a homogeneous sand for different damage levels induced by cyclic
504 loading and expressed in terms of peak cap displacement ductility. The configuration of the experiment is
505 representative of a pile group with end bearing on rock/stiff substrata. The experimental results presented in this study
506 could be used to validate three-dimensional nonlinear finite-element models for evaluating the peak ductility capacity
507 and the residual vertical load-carrying capacity of scoured pile groups damaged by earthquakes under different
508 conditions than those used in the experiments reported here. Further studies are needed to quantify the impacts of
509 different soil conditions and profiles, pile layouts, material properties, and scour depths on the residual vertical load-
510 carrying capacity of scoured pile groups damaged by earthquakes.

511 **Data Availability Statement**

512 Some or all data, models, or code that support the findings of this study (including the section analysis executable
513 codes and the force-displacement data for the pile group specimens) are available from the corresponding author upon

514 reasonable request.

515 **Acknowledgements**

516 The authors gratefully acknowledge the funding support of this work by the National Natural Science Foundation of
517 China (Grant No. 51778469). The first author is thankful for the financial support from the China Scholarship Council.
518 Any opinions, findings, and conclusions expressed are those of the authors, and do not necessarily reflect those of the
519 sponsoring organizations. All staff members in the Multi-Functional Shaking Table Laboratory of Tongji University
520 at Jiading Campus are also gratefully acknowledged.

521 **References**

- 522 ACI (American Concrete Institute). 2014. *Building code requirements for structural concrete*. ACI 318-14, Farmington
523 Hills, MI: ACI.
- 524 Banerjee, S., Stanton, J. F., and Hawkins, N. M. 1987. "Seismic performance of precast prestressed concrete piles." *J.*
525 *Struc. Eng.* 113(2), 381–396. [https://doi.org/10.1061/\(ASCE\)0733-9445\(1987\)113:2\(381\)](https://doi.org/10.1061/(ASCE)0733-9445(1987)113:2(381)).
- 526 Barbato, M., Gu, Q., and Conte, J. P. 2010. "Probabilistic push-over analysis of structural and soil-structure systems." *J.*
527 *Struc. Eng.* 136(11), 1330–1341. [https://doi.org/10.1061/\(ASCE\)ST.1943-541X.0000231](https://doi.org/10.1061/(ASCE)ST.1943-541X.0000231).
- 528 Bhattacharya, S., Blakeborough, A., and Dash, S. 2008. "Learning from collapse of piles in liquefiable soils." *Proc. Inst.*
529 *Civ. Eng. - Civ. Eng.* 161(6), 54–60. <https://doi.org/10.1680/cien.2008.161.6.54>.
- 530 Blanco, G., Ye, A., Wang, X., and Goicolea, J. M. 2019. "Parametric pushover analysis on elevated RC pile-cap
531 foundations for bridges in cohesionless soils." *J. Bridg. Eng.* 24(1), 04018104.
532 [https://doi.org/10.1061/\(ASCE\)BE.1943-5592.0001328](https://doi.org/10.1061/(ASCE)BE.1943-5592.0001328).
- 533 Chai, Y. H., and Hutchinson, T. C. 2002. "Flexural strength and ductility of extended pile-shafts II: experimental study."
534 *J. Struc. Eng.* 128(5), 595–602. [https://doi.org/10.1061/\(ASCE\)0733-9445\(2002\)128:5\(595\)](https://doi.org/10.1061/(ASCE)0733-9445(2002)128:5(595)).
- 535 Elwood, K. J., and Moehle, J. P. 2005. "Axial capacity model for shear-damaged columns." *ACI Struct. J.* 102(4), 1–37.
536 <https://doi:10.14359/14562>.
- 537 Filippou, F. C., Popov, E. P., and Bertero, V. V. 1983. *Effects of bond deterioration on hysteretic behaviour of reinforced*
538 *concrete joints*. Earthquake Engineering Research Center, University of California, Berkeley.
- 539 Guan, Z., Zhang, J., and Li, J. 2017. "Multilevel performance classifications of tall RC bridge columns toward

540 postearthquake rehabilitation requirements.” *J. Bridg. Eng.* 22(10), 04017080.
541 [https://doi.org/10.1061/\(ASCE\)BE.1943-5592.0001111](https://doi.org/10.1061/(ASCE)BE.1943-5592.0001111).

542 Hose, Y. D., and Seible, F. 1999. *Performance evaluation database for concrete bridge components and systems under*
543 *simulated seismic loads*. Pacific Earthquake Research Center, PEER 11, Berkeley, CA.

544 Kawashima, K., Takahashi, Y., Ge, H., Wu, Z., and Zhang, J. 2009. “Reconnaissance report on damage of bridges in
545 2008 Wenchuan, China, earthquake.” *J. Earthq. Eng.* 13(7), 965–996. <https://doi.org/10.1080/13632460902859169>.

546 Lam, S. S. E., Wu, B., Wong, Y. L., Wang, Z. Y., Liu, Z. Q., and Li, C. S. 2003. “Drift capacity of rectangular reinforced
547 concrete columns with low lateral confinement and high-axial load.” *J. Struc. Eng.* 129(6), 733–742.
548 [https://doi.org/10.1061/\(ASCE\)0733-9445\(2003\)129:6\(733\)](https://doi.org/10.1061/(ASCE)0733-9445(2003)129:6(733)).

549 Lemnitzer, A., Khalili-Tehrani, P., Ahlberg, E. R., Rha, C., Taciroglu, E., Wallace, J. W., and Stewart, J. P. 2010.
550 “Nonlinear efficiency of bored pile group under lateral loading.” *J. Geotech. Geoenvironmental Eng.* 136(12),
551 1673–1685. [https://doi.org/10.1061/\(ASCE\)GT.1943-5606.0000383](https://doi.org/10.1061/(ASCE)GT.1943-5606.0000383).

552 Lin, S.-S., and Liao, J.-C. 1999. “Permanent strains of piles in sand due to cyclic lateral loads.” *J. Geotech.*
553 *Geoenvironmental Eng.* 125(9), 798–802. [https://doi.org/10.1061/\(ASCE\)1090-0241\(1999\)125:9\(798\)](https://doi.org/10.1061/(ASCE)1090-0241(1999)125:9(798)).

554 Liu, T., Wang, X., and Ye, A. 2020. “Roles of pile group and cap-rotation effects on seismic failure mechanisms of
555 partially-embedded bridge foundations: Quasi-static tests.” *Soil Dyn. Earthq. Eng.* 132, 106074.
556 <https://doi.org/10.1016/j.soildyn.2020.106074>.

557 Mander J.B., Dutta A., and Goel P. 1998. *Capacity design of bridge piers and the analysis of overstrength*. MCEER-98-
558 0003.

559 Mazzoni, S., McKenna, F., Scott, M. H., and Fenves, G. L. 2006. *OpenSees command language manual*. Pacific
560 Earthquake Engineering Research Center, Berkeley, CA.

561 McKenna, F. 2011. “OpenSees: A framework for earthquake engineering simulation.” *Comput. Sci. Eng.* 13(4), 58–66.
562 <https://doi.10.1109/MCSE.2011.66>.

563 O’Connor, J., and Alampalli, S. 2010. “Post-earthquake bridge inspection guide lines for NewYork state.” *Bridg.*
564 *Maintenance, Safety, Manag. Life-Cycle Optim. - Proc. 5th Int. Conf. Bridg. Maintenance, Saf. Manag.* 160–160.

565 Park, R., and Falconer, T. J. 1983. “Ductility of prestressed concrete piles subjected to simulated seismic loading.” *PCI J.*

566 28(5), 112–144. <https://doi:10.15554/pcij.09011983.112.144>.

567 Rollins, K. M., Johnson, S. R., Petersen, K. T., and Weaver, T. J. 2003. “Static and dynamic lateral load behavior of pile
568 groups based on full-scale testing.” *Proc. Int. Offshore Polar Eng. Conf.*, International Society of Offshore and
569 Polar Engineers.

570 Rollins, K. M., Lane, J. D., and Gerber, T. M. 2005. “Measured and computed lateral response of a pile group in sand.” *J.*
571 *Geotech. Geoenvironmental Eng.* 131(1), 103–114. [https://doi.org/10.1061/\(ASCE\)1090-0241\(2005\)131:1\(103\)](https://doi.org/10.1061/(ASCE)1090-0241(2005)131:1(103)).

572 Rollins, K. M., Olsen, K. G., Jensen, D. H., Garrett, B. H., Olsen, R. J., and Egbert, J. J. 2006. “Pile spacing effects on
573 lateral pile group behavior: analysis.” *J. Geotech. Geoenvironmental Eng.* 132(10), 1272–1283.
574 [https://doi.org/10.1061/\(ASCE\)1090-0241\(2006\)132:10\(1272\)](https://doi.org/10.1061/(ASCE)1090-0241(2006)132:10(1272)).

575 Scott, B. D., Park, R., and Priestley, M. J. N. 1982. “Stress-strain behavior of concrete confined by overlapping hoops at
576 low and high strain rates.” *ACI J. Proc.* 79(1), 13–27. <https://doi:10.14359/10875>.

577 Shang, Y., Alipour, A., and Ye, A. 2018. “Selection of input motion for seismic analysis of scoured pile-supported bridge
578 with simplified models.” *J. Struct. Eng.* 144(8), 04018099. [https://doi.org/10.1061/\(ASCE\)ST.1943-541X.0002067](https://doi.org/10.1061/(ASCE)ST.1943-541X.0002067).

579 Tasai, A. 2000. *Residual axial capacity of reinforced concrete columns during shear degradation*. Pacific Earthquake
580 Engineering Research Center, PEER 10, Berkeley, CA, 257-267.

581 Terzic, V., and Stojadinovic, B. 2015a. “Evaluation of post-earthquake axial load capacity of circular bridge columns.”
582 *ACI Struct. J.* 112(1), 23–34. <https://doi:10.14359/51687296>.

583 Terzic, V., and Stojadinovic, B. 2015b. “Calibration and validation of analytical models for predicting the seismic and
584 axial-load response of circular bridge columns.” *J. Bridg. Eng.* 20(9), 04014098.
585 [https://doi.org/10.1061/\(ASCE\)BE.1943-5592.0000702](https://doi.org/10.1061/(ASCE)BE.1943-5592.0000702).

586 Wang, S.-C., Liu, K.-Y., Chen, C.-H., and Chang, K.-C. 2015. “Experimental investigation on seismic behavior of
587 scoured bridge pier with pile foundation.” *Earthq. Eng. Struct. Dyn.* 44(6), 849–864.
588 <https://doi.org/10.1002/eqe.2489>.

589 Wang, X., Fang, J., Zhou, L., and Ye, A. 2019a. “Transverse seismic failure mechanism and ductility of reinforced
590 concrete pylon for long span cable-stayed bridges: Model test and numerical analysis.” *Eng. Struct.* 189, 206–221.
591 <https://doi.org/10.1016/j.engstruct.2019.03.045>.

592 Wang, X., Shafieezadeh, A., and Ye, A. 2019b. "Optimal EDPs for post-earthquake damage assessment of extended pile-
593 shaft-supported bridges subjected to transverse spreading." *Earthq. Spectra*, 35(3), 1367–1396.
594 <https://doi.org/10.1193/090417EQS171M>.

595 Wang, X., Ye, A., He, Z., and Shang, Y. 2016. "Quasi-static cyclic testing of elevated rc pile-cap foundation for bridge
596 structures." *J. Bridg. Eng.* 21(2), 04015042. [https://doi.org/10.1061/\(ASCE\)BE.1943-5592.0000797](https://doi.org/10.1061/(ASCE)BE.1943-5592.0000797).

597 Wang, X., Ye, A., and Ji, B. 2019c. "Fragility-based sensitivity analysis on the seismic performance of pile-group-
598 supported bridges in liquefiable ground undergoing scour potentials." *Eng. Struct.* 198, 109427.
599 <https://doi.org/10.1016/j.engstruct.2019.109427>.

600 Wang, X., Ye, A., Shang, Y., and Zhou, L. 2019d. "Shake-table investigation of scoured RC pile-group-supported
601 bridges in liquefiable and nonliquefiable soils." *Earthq. Eng. Struct. Dyn.* 48(11), 1217–1237.
602 <https://doi.org/10.1002/eqe.3186>.

603 Wang, Z., Dueñas-Osorio, L., and Padgett, J. E. 2014. "Influence of scour effects on the seismic response of reinforced
604 concrete bridges." *Eng. Struct.* 76, 202–214. <https://doi.org/10.1016/j.engstruct.2014.06.026>.

605 Wardhana, K., and Hadipriono, F. C. 2003. "Analysis of recent bridge failures in the united states." *J. Perform. Constr.*
606 *Facil.* 17(3), 144–150. [https://doi.org/10.1061/\(ASCE\)0887-3828\(2003\)17:3\(144\)](https://doi.org/10.1061/(ASCE)0887-3828(2003)17:3(144)).

607 Wei, X., Wang, Q., and Wang, J. 2008. "Damage patterns and failure mechanisms of bridge pile foundation under
608 earthquake." *14th World Conf. Earthq. Eng.*, Beijing, China.

609 Yeh, Y.-K., Mo, Y. L., and Yang, C. Y. 2002. "Seismic performance of rectangular hollow bridge columns." *J. Struct.*
610 *Eng.* 128(1), 60–68. [https://doi.org/10.1061/\(ASCE\)0733-9445\(2002\)128:1\(60\)](https://doi.org/10.1061/(ASCE)0733-9445(2002)128:1(60)).

611 Zhou, L., Wang, X., and Ye, A. 2019. "Shake table test on transverse steel damper seismic system for long span cable-
612 stayed bridges." *Eng. Struct.* 179, 106–119. <https://doi.org/10.1016/j.engstruct.2018.10.073>.

613

614

615

Tables

616

Table 1. Mechanical properties of concrete and steel reinforcements

Material	Elastic modulus (MPa)	Yield strength (MPa)	Peak strength (MPa)	Strain corresponding to peak strength
Concrete	32260 (3.2%)	--	25.2 (1.6%)	--
ϕ6mm rebars	216353 (5.1%)	429 (3.7%)	670 (3.2%)	0.120 (2.1%)
ϕ3.5mm GIW	135441 (6.3%)	317 (4.0%)	421 (2.2%)	0.148 (11.2%)

Note: data in the parentheses refer to the variation coefficient.

617

618

Table 2. Test matrix

Specimen	Lateral damage state target	Peak lateral disp./mm	Test sequences
#1	First yielding of belowground pile shaft	35	Lateral and vertical
#2	Onset of lateral strength degradation (or peak strength)	70	Lateral and vertical
#3	15% lateral strength degradation	100	Lateral and vertical

619

620

Table 3. Pile head curvatures calculated through the data from linear potentiometers

Loading direction	Disp. level (mm)	Curvatures (rad/m)		
		Pile 1	Middle pile	Pile 3
Push	+35	-0.196	-0.103	-0.150
	+70	-0.570	-0.398	-0.319
	+100	-0.923	-0.604	-0.449
Pull	-35	0.134	0.142	0.247
	-70	0.362	0.379	0.498
	-100	0.556	0.666	0.825

621

622

Table 4. Peak displacement and curvature ductility of the test specimens

Specimen	Lateral damage state	Displacement ductility	Maximum curvature ductility of first aboveground plastic hinge
#1	First belowground yielding of pile shaft	1.75	5.49
#2	Onset of lateral strength degradation	3.50	12.67
#3	15% lateral strength degradation	5.00	20.51

623

624

625

Table 5. Global performance and local damage descriptions for the pile group specimens

Specimen	Performance description	Peak displacement ductility	Residual cap displacement (mm)	Residual cap rotation ($\text{rad} \times 10^{-3}$)	Residual crack width (mm)	Observed aboveground pile damage description
#1	First belowground yielding	1.75	14	0.0	0.28	Hairline residual cracks near pile head regions
#2	Onset of lateral strength degradation	3.50	40	0.7	0.98	Slight concrete spalling at pile head
#3	15% lateral strength degradation	5.00	68	3.9	--	Extensive cover concrete spalling and local core concrete crushing

626 Note: The residual crack width was measured on the leading pile at the west side of the specimens at approximately 8 cm below the pile
627 head.

628

629

Figure captions

630

631 Figure 1. Quasi-static test overview and instrumentations: (a) side view of schematic diagram, (b) plan view of
632 schematic diagram, (c) pile reinforcement and strain gage distribution over a single pile, and (d) single pile cross-
633 section (all units are in cm if not otherwise indicated)

634 Figure 2. Photographs of physical test layout: (a) full-view, (b) actuator-cap connections, (c) sand and aboveground
635 piles, (d) laser sensor positions, and (e) inclinometer

636 Figure 3. Numerical moment-curvature response of a pile cross-section subjected to an axial load ratio of 5%

637 Figure 4. Particle size distribution of test sand

638 Figure 5. Loading protocols

639 Figure 6. Comparison of soil pressures on leading pile and container walls

640 Figure 7. Lateral hysteretic behavior of specimens: (a) force versus displacement curves, and (b) envelope curves

641 Figure 8. Curvature distributions of piles at positive (push) and negative (pull) peak displacements for different
642 loading cycles

643 Figure 9. Cap rotation angle: (a) versus peak lateral displacement (pull and push directions), and (b) versus
644 displacement ductility (only positive quadrant)

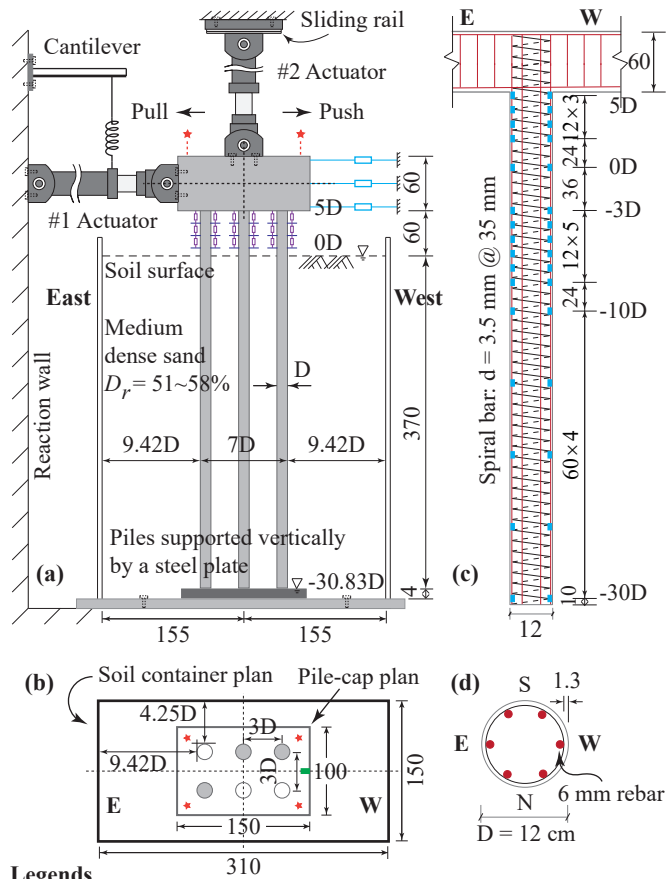
645 Figure 10. Variations of crack width at the leading pile head: (a) hysteretic lateral force versus crack width curves,
646 and (b) comparison of crack width at different loading states

647 Figure 11. Observed physical damage of the pile group specimens at the end of the corresponding lateral loading (or
648 residual deformation state): (a) specimen #1, (b) specimen #2, and (c) specimen #3

649 Figure 12. Axial force-strain curves for the short columns

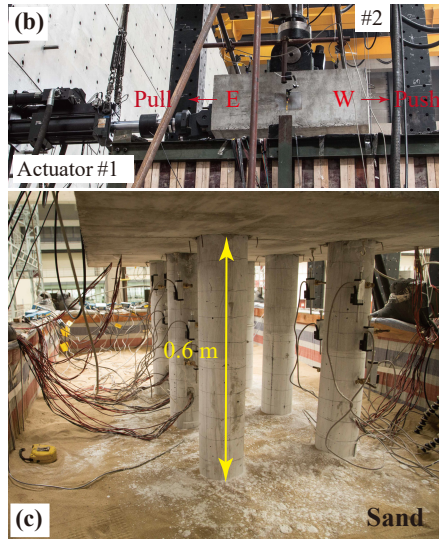
650 Figure 13. Residual vertical load-carrying capacity of pile group foundations under different damage levels: (a)
651 vertical load versus vertical displacement increment, and (b) lateral displacement versus vertical displacement
652 increment

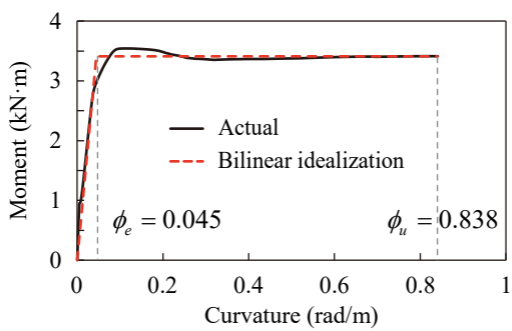
- 653 Figure 14. Post-test observations of the physical specimens after soil removal: (a) specimen #1, (b) specimen #2, and
654 (c) specimen #3
- 655 Figure 15. Vertical load capacity degradation data and fitting curve

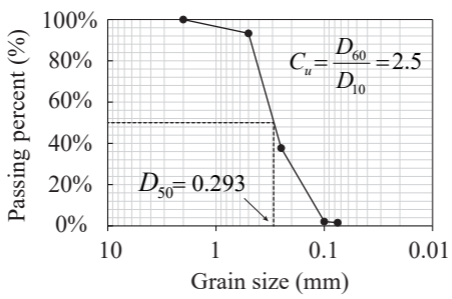


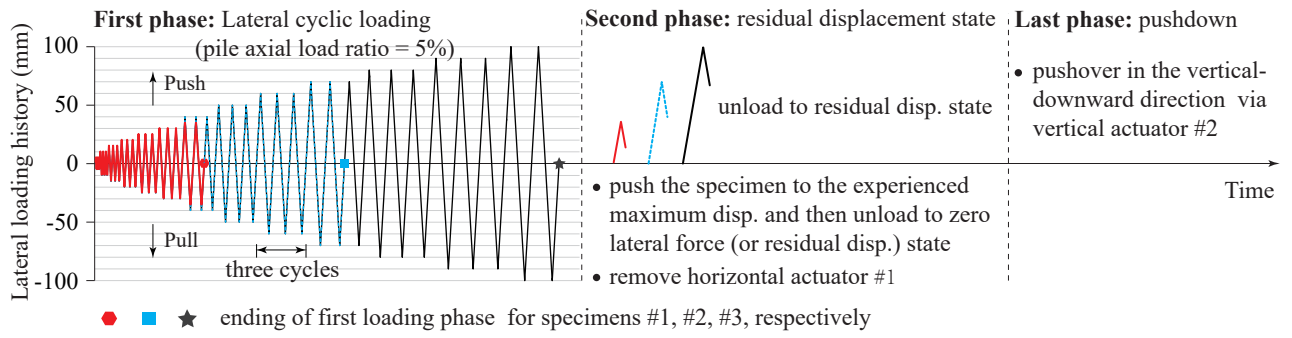
Legends

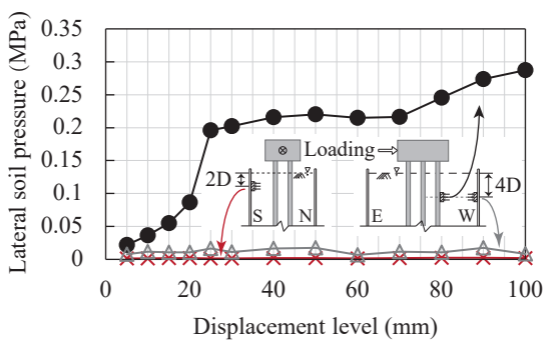
- Piles with strain gauges and linear potentiometers
- ★ Laser sensor
- LVDT
- ▭ Linear potentiometers
- Strain gauge
- Inclinometer

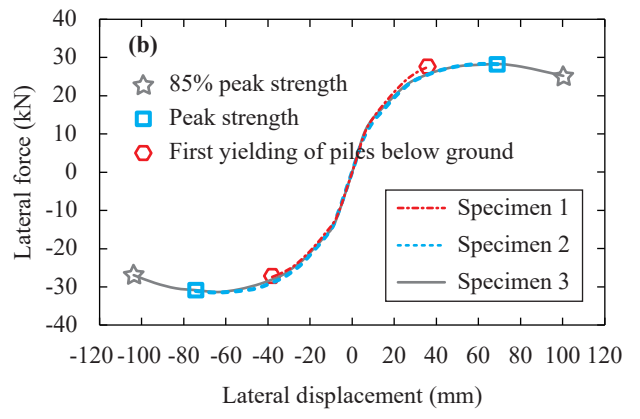
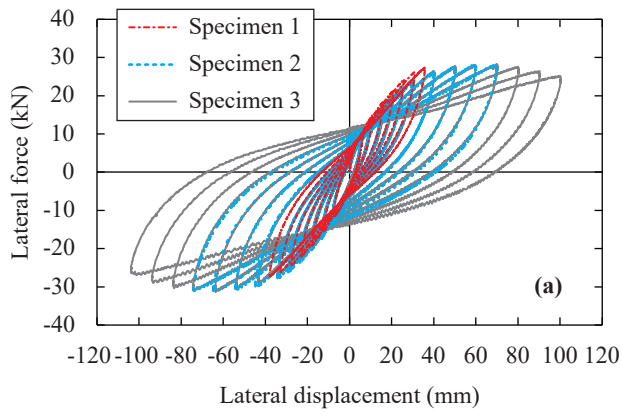




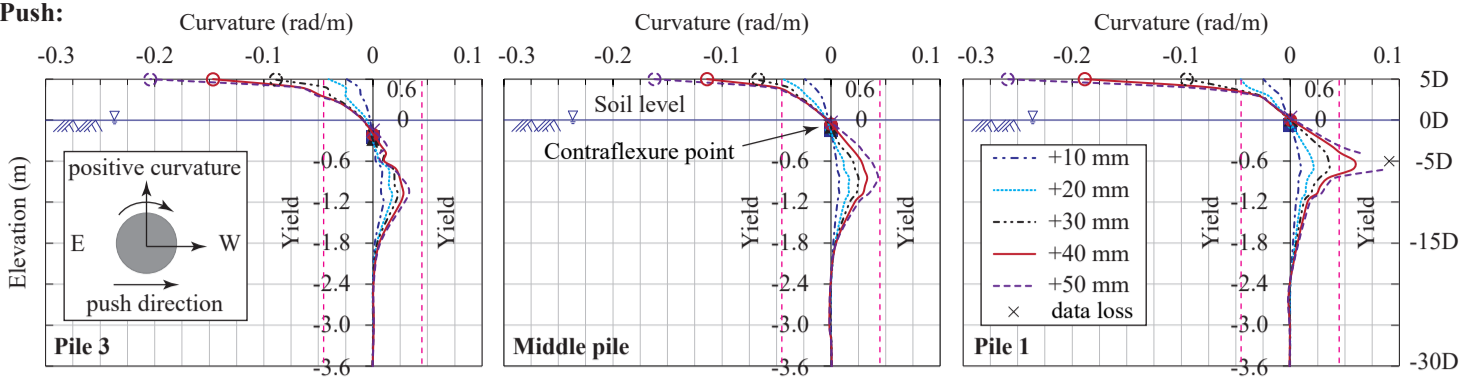




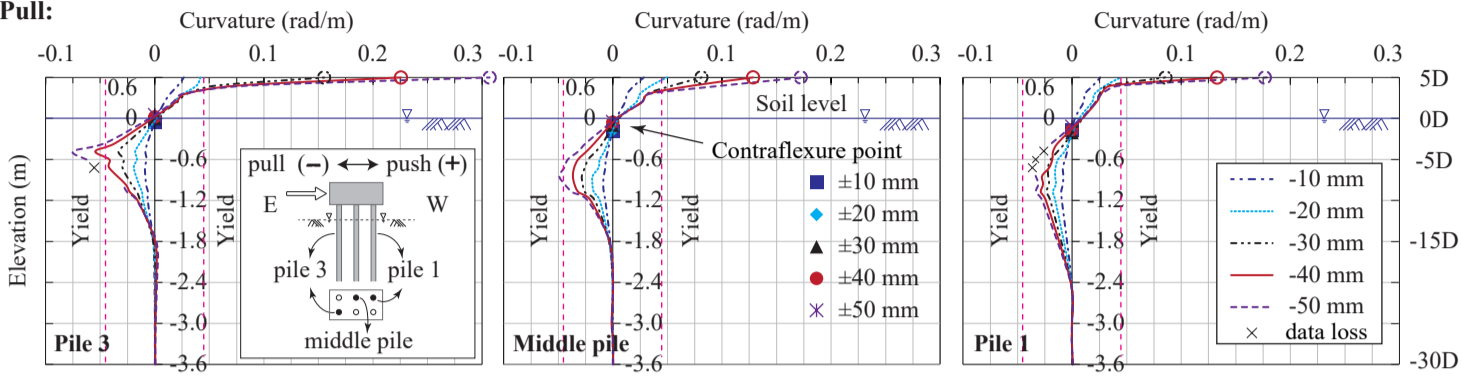


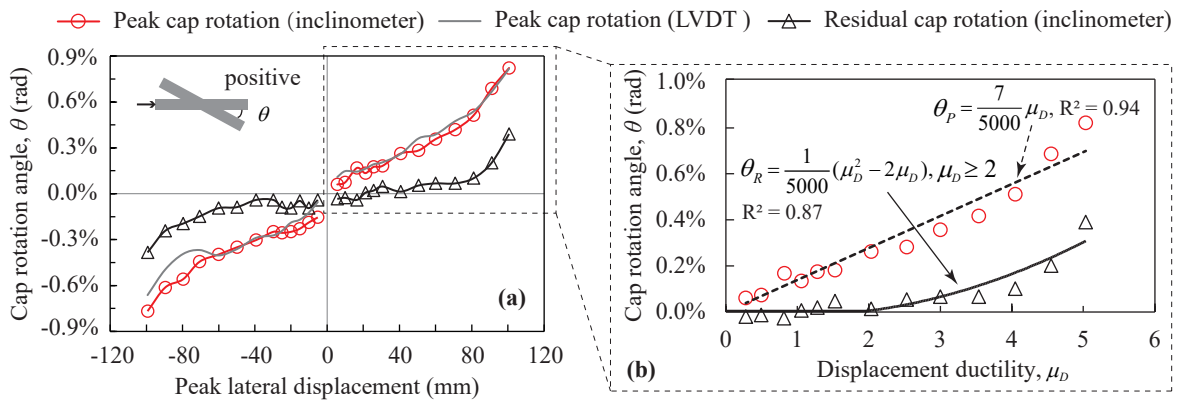


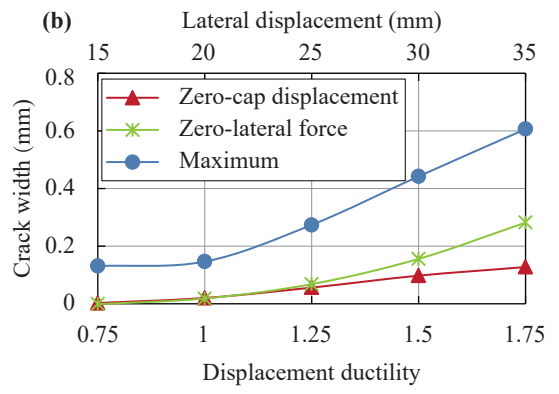
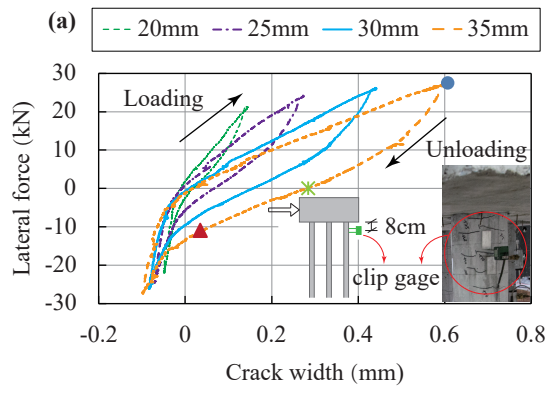
Push:

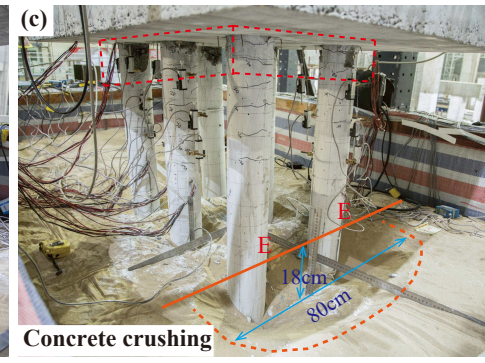
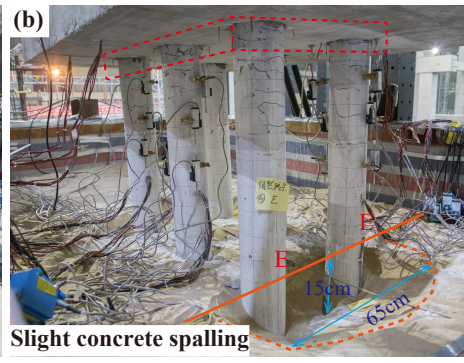
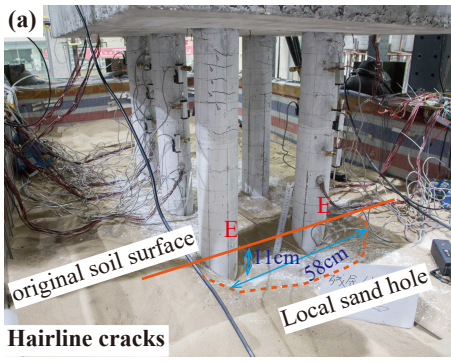


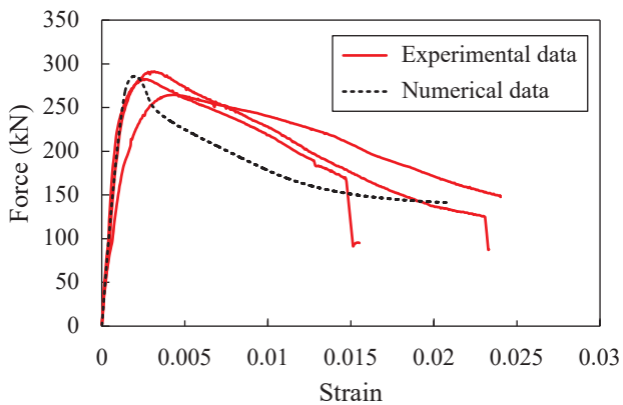
Pull:

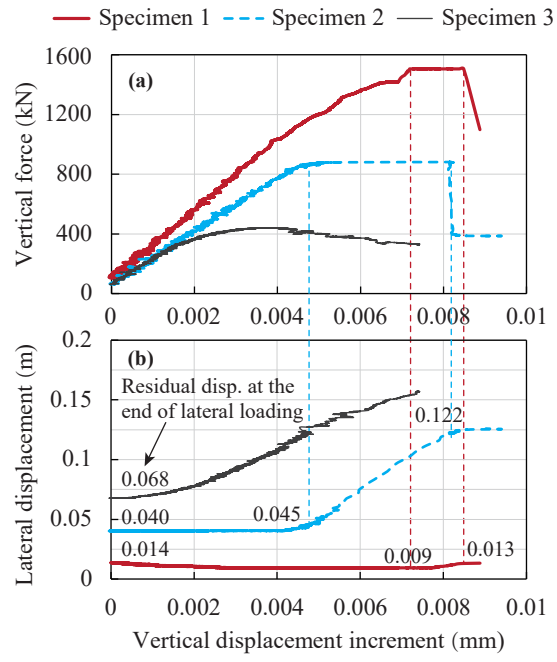


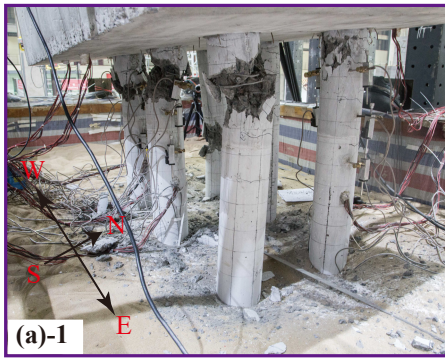








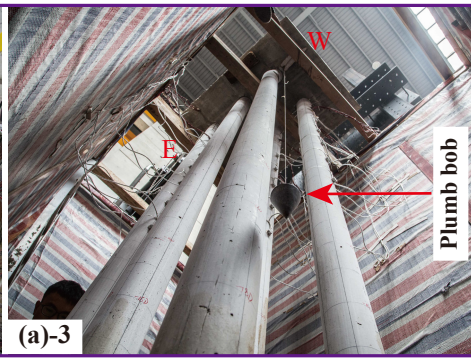




(a)-1



(a)-2



(a)-3



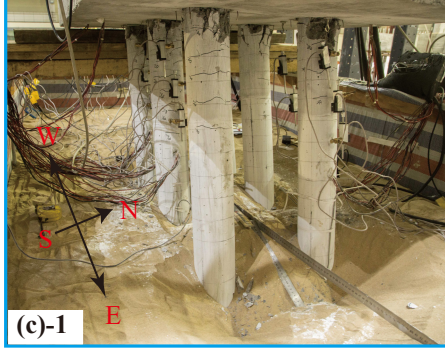
(b)-1



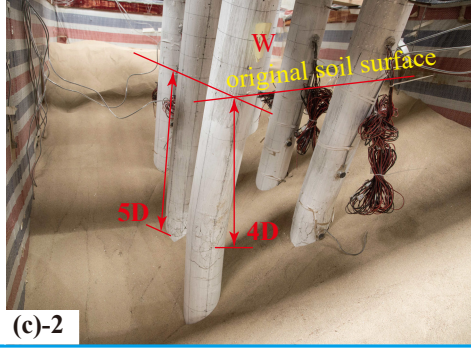
(b)-2



(b)-3



(c)-1



(c)-2



(c)-3

